Laser-Assisted Etching of Manganese-Zinc-Ferrite

Edward K. Yung,*,[1] Brian W. Hussey, Arunava Gupta,* and Lubomyr T. Romankiw*

IBM Thomas J. Watson Research Center, Yorktown Heights, New York 10598

ABSTRACT

A focused argon ion laser beam (514.5 nm) has been used to induce etching of manganese-zinc-ferrite ceramics in aqueous KOH solutions. In the absence of the laser beam the etching process did not take place even at the boiling point of the selected etchant. For KOH concentration above 2*N*, bubble-free etching took place in the presence of the laser beam. Within the range of 2-8*N* for KOH concentration, the depth of the etched grooves increased with increasing laser power, decreasing scan speed, and increasing KOH concentration. Evidence of decreasing average etch rate due to mass transport limitation was observed under low KOH concentration, high laser power, and low scan speed conditions. The width of the etched grooves increased with increasing laser power, but was relatively insensitive to the scan speed and the KOH concentration. The experimental findings of the laser-assisted etching of Mn-Zn-ferrite can be qualitatively interpreted by a thermally activated reaction mechanism: formation at and above a threshold temperature of an active chemical environment on the surface for the initiation of the etching process; more concentrated etchant allows more abundant supply of the reactive species and requires less heat input to reach the active state. Etching of ferrite occurs as a result of the reaction between the active etchant (possibly fused KOH) and either the solid or the molten ferrite, depending on the laser power. The etching process generates soluble product species and the profiles of the etched patterns are strongly influenced by the mass transport characteristics of the etching system. A mathematical model for the surface temperature distribution, which takes into account heat loss into the liquid, is also presented.

Laser-assisted etching of a wide variety of metals, insulators, semiconductors, and organics have been reported in recent years (1). The laser radiation initiates and/or enhances the etching process by photochemical or photothermal effect at the surface. Etching takes place either due to decomposition and volatilization of the material, or due to reaction at the surface with a gaseous or liquid reactant to form volatile or soluble species. Most of the work on laser etching which has been reported in the literature involves etching in the gas phase, or direct ablation of material (1). Wet etching in the presence of a laser has been used successfully for etching of GaAs in an aqueous solutions of HF, HNO_3, and H_2SO_4/H_2O_2 mixture, to produce deep via holes and submicrometer gratings (2). Rapid etching of Si in KOH and NaOH solutions, in the presence of a focused visible or infrared laser, has also been reported (3, 4). It has been suggested that the melting of the Si and the increase in mass transport due to microstirring result in enhanced etch rates (3). A focused argon ion laser beam with relatively high intensity ($\sim 10^6$ W/cm^2) has been used for etching of Al_2O_3/TiC ceramics in KOH solution (3). The etching is enhanced due to melting and vaporization of the ceramic. Efficient etching of modified $PbTiO_3$ ceramics in KOH solution using an argon ion laser has also been reported (5).

We have investigated the thermal etching characteristics of a magnetic oxide, manganese-zinc-ferrite, in KOH solution using a focused argon ion laser beam. The high relative permeability and saturation magnetization, along with the high electrical resistivity, of manganese-zinc-ferrites makes them useful for a wide range of applications, including magnetic core memories, inductors, and recording heads (6). They have the mixed spinel structure, $Mn_{1-x}Zn_xFe_{2+\delta}O_4$ (7), where the magnetic moment can be tailored by changing the relative concentration of Mn^{+2} and Zn^{+2}. A slight excess of iron (as Fe^{+2}) is present in order to optimize permeability and magnetic saturation. The composition of the ferrite material used in the present study was $Mn_{0.6}Zn_{0.4}Fe_{2.3}O_4$. The material was prepared by standard ceramic processing of ferrite and was subsequently polished. The term "ferrite" appearing in the text refers to this particular manganese-zinc-ferrite material.

There is very little work reported in the open literature on suitable etchants for Mn-Zn-ferrite. A mixture of 10% H_2SO_4 and Zn powder has been used for etching certain compositions of the ferrite material (8). Recently, Uemura *et al.* (9) have reported using hot phosphoric acid to etch Mn-Zn-ferrite crystals with various chemical composition. We selected aqueous KOH solution for efficient etching of Mn-Zn-ferrite when locally heated with a laser. According to the Pourbaix diagrams (10), soluble complex species of all three oxide components of the Mn-Zn-ferrite can be formed in high *p*H aqueous solutions. Chemical etching of the Mn-Zn-ferrite, however, does not occur without the laser even at the boiling point of the aqueous KOH solutions. Experimental verification of the reaction between molten KOH and Mn-Zn-ferrite was not attempted.

Experimental

The schematics of our experimental system is illustrated in Fig. 1. The TEM_{00} output at 514.5 nm from an Ar^+ laser (Coherent, Innova 20) was used as the excitation source for the wet etching process under investigation. The etchant selected for the experiments was aqueous KOH of variable concentrations. At this wavelength, the absorption of the laser beam energy by the KOH etchant is minimal. Additionally, the laser power is expected to be fully absorbed by the ferrite substrate, especially after initial surface roughening due to the etching action that has taken place. The laser beam was focused, using a microscope (Cambridge Instruments) with a 5 times (NA 0.09) objective lens (Leitz Wetzlar), on the substrate placed in a sample holder which was mounted onto a scanning X-Y stage (Compumotor Corporation). The base of the sample holder was polished and was kept flat to assure that the ferrite surface stayed in focus throughout the course of the scanning experiment. A built-in 80-20% (nominal specification) beamsplitter, located before the objective lens, provided a side beam whose power was measured (Coherent, Model 212 power meter, or PAR, Model 460-1A power meter with 550-11 attenuator). An attenuator (CVI Laser Corporation Model AAT75-51L) was placed in the light path for manual

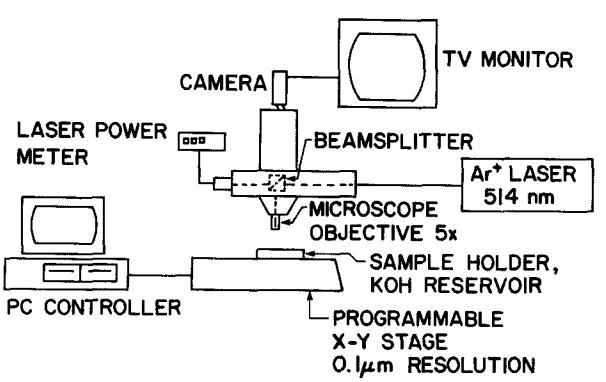

Fig. 1. Schematic diagram of the experimental setup for etching Mn-Zn-ferrite.

*Electrochemical Society Active Member.
[1]Present address: Microelectronic Center of North Carolina, Research Triangle Park, North Carolina 27709.

adjustment of the laser power entering the optical unit. A video camera was mounted on top of the optic column, and the video image was sent to a B/W monitor for focusing check and for real time process monitoring. The motion of the X-Y stage was controlled by an IBM PC, with an option for manual control. Both the X- and Y-motors had a 0.1 μm resolution and could achieve a maximum scan speed of 1 cm/s. The entire experimental system, with the exception of the laser power supply and the control units for the X-Y stage, was mounted on an optical bench to minimize effects due to floor vibration.

After the etching experiment the ferrite piece was water rinsed and dried. The width of the etched grooves was measured using a calibrated optical microscope. Except for shallow grooves with depth less than ~2000Å, the boundaries of the etched grooves were usually sharp and measurement of the width of the etched grooves could easily be made. Depth measurements were carried out by a surface profile analyzer (Sloan Dektak 3030) equipped with a submicron stylus. However, profilometric depth measurement for deep grooves could be erroneous due to restricted penetration of the stylus. In a few experiments where deep grooves were etched, both the SEM micrographs and the Dektak measurements were taken. Comparison between the Dektak data and the SEM micrographs indicated that, when the stylus was kept clean, the depth readings from the profilometer were accurate, up to ~16 μm, for grooves etched with the 5 times objective lens.

Thermal Model

Generally speaking, etching kinetics is strongly temperature dependent. Consequently, it is highly desirable to either experimentally measure, or to theoretically compute, the surface temperature distribution for the interpretation of the observed etching behavior. At present, there is no satisfactory experimental technique known to us that can resolve the temperature distribution in a micron-sized region under laser illumination. Therefore, a model was developed to compute the temperature on the ferrite surface.

The basic assumptions for our model are:

1. The stationary Ar^+ cw laser beam has a gaussian intensity distribution.
2. The substrate is moving at a constant speed u along the $+x$ direction.
3. The ferrite material is isotropic and its physical properties (ρ, C_p, κ, λ, etc.) are temperature-independent. Although our model is constructed on the basis of temperature-independent thermal properties, the result can easily be applied, through the Kirchoff transformation (11), to the case where the ferrite thermal properties vary in a known fashion with temperature.
4. Melting of bulk ferrite does not occur under the Ar^+ laser illumination and a fused salt layer, if present during the etching process, is of negligible thickness. This assumption enables us to use the thermal properties of solid ferrite in our computation. Molten ferrite may have thermal properties vastly different from those of solid ferrite, and consequently the temperature distribution may deviate from that predicted by this model. Since in most of our etching experiments the presence of molten ferrite was not visually detected, this assumption is considered valid.
5. The interaction between the laser beam and the ferrite substrate is purely thermal.
6. The laser beam energy is completely absorbed by the ferrite substrate.
7. Power absorption by the bulk ferrite is represented by Beer-Lambert's law.
8. There is no power loss due to absorption of the laser wavelength light by the KOH etchant.
9. Heat of reaction, as compared to the extremely high energy density of the laser beam, has negligible effect on the temperature distribution.
10. The ferrite substrate is treated as a semi-infinite domain.
11. Heat loss into the liquid is represented by the "radiation" boundary condition, *i.e.*, the heat loss rate is the temperature difference times the heat transfer coefficient, H, which is assumed to be a constant.

The rectangular coordinates, which are fixed in space as well as being fixed with respect to the stationary laser beam, are selected as the basis for formulation of our model. The origin is on the ferrite surface (x-y plane) and is directly underneath the beam center. The positive z-axis points into the bulk substrate. The positive x-axis is in the direction of the motion of the substrate.

The heat equation is

$$\rho C_p \frac{\partial T}{\partial t} = \kappa \left(\frac{\partial^2 T}{\partial x^2} + \frac{\partial^2 T}{\partial y^2} + \frac{\partial^2 T}{\partial z^2} \right) - u \rho C_p \frac{\partial T}{\partial x} - \frac{\partial I}{\partial z} \qquad [1]$$

where

$$\frac{\partial I}{\partial z} = \frac{-P}{\pi w^2 \lambda} e^{-\frac{x^2}{w^2} - \frac{y^2}{w^2} - \frac{z}{\lambda}} \qquad [2]$$

and $T(x, y, z, t)$ is the temperature rise above room temperature. Equation [1] is valid for

$$-\infty < x \text{ and } y < \infty;\ 0 \le z < \infty;\ t > 0$$

The boundary conditions are

$$T = 0 \text{ at } t = 0$$

$$T \to 0 \text{ as } x, y \to \pm \infty$$

$$T \to 0 \text{ as } z \to \infty$$

$$\frac{\partial T}{\partial z} = \frac{H}{\kappa} T \text{ at } z = 0$$

We define the following dimensionless variables

$$X = \frac{x}{w},\quad Y = \frac{y}{w},\quad Z = \frac{z}{w},\quad \alpha = \frac{w}{\lambda}$$

$$\tau = \frac{tD}{w^2} \quad \text{where } D = \frac{\kappa}{\rho C_p}$$

$$\mu = \frac{uw}{D}$$

$$\Psi = \frac{T}{\Delta T}, \quad \text{where } \Delta T = \frac{P}{2\sqrt{\pi}\,\kappa w}$$

$$\Theta = \frac{wH}{\kappa}$$

The dimensionless heat equation is

$$\frac{\partial \Psi}{\partial \tau} = \frac{\partial^2 \Psi}{\partial X^2} + \frac{\partial^2 \Psi}{\partial Y^2} + \frac{\partial^2 \Psi}{\partial Z^2} - \mu \frac{\partial \Psi}{\partial X} + \frac{2\alpha}{\sqrt{\pi}} e^{-X^2 - Y^2 - \alpha Z} \qquad [3]$$

and the dimensionless boundary conditions are

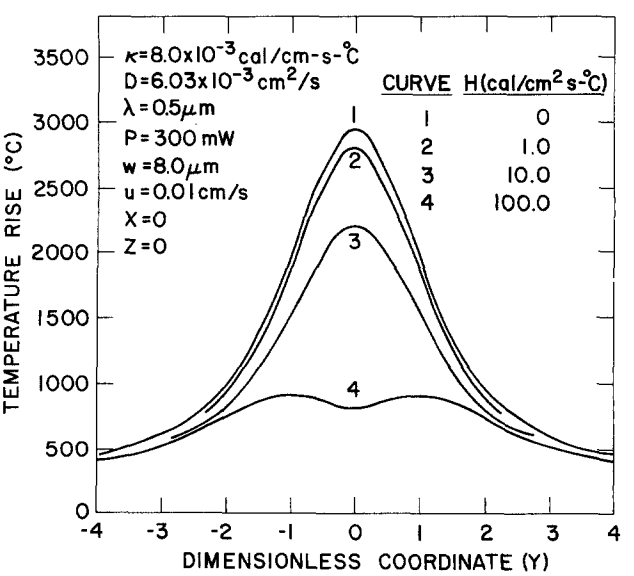

Fig. 2. Computed temperature profiles for different rates of convective heat loss.

$$\Psi = 0 \text{ at } \tau = 0$$

$$\Psi \to 0 \text{ as } X\ Y \to \pm\infty$$

$$\Psi \to 0 \text{ as } Z \to \infty$$

$$\frac{\partial \Psi}{\partial z} = \Theta\Psi \text{ at } Z = 0$$

In our analysis, the Green's function method is used. The Green's function $G(X, Y, Z, \tau, X', Y', Z', \tau')$ for the dimensionless heat equation is (12)

$$G = \frac{1}{[4\pi(\tau - \tau')]^{3/2}} e^{\left[\frac{-\{[X - X' - \mu(\tau - \tau')]^2 + (Y - Y')^2\}}{4(\tau - \tau')}\right]} x \left\{ e^{\frac{Z - Z'}{4(\tau - \tau')}} + e^{\frac{Z + Z'}{4(\tau - \tau')}} - 4\pi(\tau - \tau')^{1/2}\Theta e^{[\Theta^2(\tau - \tau') + \Theta(Z + Z')]} \operatorname{erfc}\left[\frac{(Z + Z')}{2\sqrt{\tau - \tau'}} + \Theta\sqrt{\tau - \tau'}\right]\right\} \quad [4]$$

The selected Green's function satisfies all boundary conditions, and the dimensionless surface temperature Ψ can be formulated as

$$\Psi(X, Y, 0, \tau) = \int_0^\tau \int_{-\infty}^{\infty} \int_{-\infty}^{\infty} \int_0^{\infty} G(X, Y, 0, \tau, X', Y', Z', \tau') \frac{2\alpha}{\sqrt{\pi}} e^{-X'^2 - Y'^2 - \alpha Z'}\, dZ' dY' dX' d\tau'$$

$$= \frac{2\alpha}{\sqrt{\pi}} \int_0^\tau \frac{1}{1 + 4\phi} e^{\alpha^2\phi} \operatorname{erfc}(\alpha\sqrt{\phi})\, e^{-\frac{[(X - \mu\phi)^2 + Y^2]}{1 + 4\phi}} d\phi - \frac{\alpha\Theta}{\sqrt{\pi}} \int_0^\tau \frac{1}{1 + 4\phi} e^{-\frac{[(X - \mu\phi)^2 + Y^2]}{1 + 4\phi}} \int_0^{\infty} e^{(\Theta^2\phi + \Theta Z')} \operatorname{erfc}\left(\frac{Z'}{2\sqrt{\phi}} + \Theta\sqrt{\phi}\right) \frac{e^{-\alpha Z'}}{\sqrt{\pi}\sqrt{\phi}} dZ' d\phi \quad [5]$$

Therefore, the temperature rise on the ferrite surface ($Z = 0$) is

$$T(X, Y, 0, \tau) = \frac{P}{2\sqrt{\pi}\,\kappa w} \Psi(X, Y, 0, \tau)$$

$$= \frac{P}{\pi\kappa\lambda} \int_0^\tau \frac{1}{1 + 4\phi} e^{\alpha^2\phi} \operatorname{erfc}(\alpha\sqrt{\phi})\, e^{-\frac{[(X - \mu\phi)^2 + Y^2]}{1 + 4\phi}} d\phi - \frac{P\Theta}{2\pi\kappa\lambda} \int_0^\tau \frac{1}{1 + 4\phi} e^{-\frac{[(X - \mu\phi)^2 + Y^2]}{1 + 4\phi}} \int_0^{\infty} e^{(\Theta^2\phi + \Theta Z')} \operatorname{erfc}\left(\frac{Z'}{2\sqrt{\phi}} + \Theta\sqrt{\phi}\right) \frac{e^{-\alpha Z'}}{\sqrt{\pi}\sqrt{\phi}} dZ' d\phi \quad [6]$$

Subroutine QA05A of the HARWELL mathematical library was selected for evaluating the single integral, and subroutine DBLIN of the IMSL library was selected for evaluating the double integral. Shown in Fig. 2 are steady-state ($\tau =$ temperature profiles for various rates of radiation loss (represented by the heat transfer coefficient, H), including the upper bound obtained for the no-loss case. As is expected, the surface temperature decreases as the heat loss to the etchant increases. Significant surface cooling (*e.g.*, temperature drop > ~20% of the peak value) only occurs for H values greater than 10.0 cal/cm^2-s-°C. For very high H value (*e.g.*, H = 100.0 in Fig. 2), the thermal loss at the beam center is greater than the energy influx from the absorption of the laser beam. In order to achieve thermal balance locally at the beam center, diffusive thermal flow toward the beam center, driven by both the surface temperature gradient between the beam center and the surrounding area and the temperature gradient into the bulk ferrite, is required. Consequently, the maximum surface temperature is off the beam center and the valley is seen in the surface temperature profile. It should be pointed out that the heat transfer coefficient "H" characterizes the overall thermal conductance from the ferrite surface into the bulk region of the etchant. Mechanisms for thermal dissipation include convection/conduction in the liquid phase as well as conduction through substances, if present, at the ferrite surface.

Assuming that thermal dissipation occurs only in the liquid phase, the heat loss rate is the product of the thermal diffusivity, D, and the temperature gradient across a thin liquid layer, called thermal boundary layer. In order to properly arrive at the thermal boundary layer thickness, the exact mechanism of the heat transfer process in the liquid medium has to be understood. Such information is generally lacking, at least for heating (or cooling) over an area of a focused laser beam. Therefore, it would not be proper for us to arbitrarily draw conclusions on the value of the heat transfer coefficient applicable to our process. Considering, as a first estimate, the case of hemispherical thermal conduction in the aqueous phase, and assuming a value of 1.46×10^{-3} cal/cm-s-°C for the thermal conductivity of water (13), and a value of 10 μm for the radius of the heated zone, the heat transfer coefficient is estimated to be 1.46 cal/cm^2-s-°C. This value is a lower bound estimate, and according to Fig. 2, thermal loss for such a H value is not significant. In a laser-heated system, if the thermal resistance lies entirely in the liquid phase, fluid motion (natural convection) can be expected as a result of the hydrodynamic instability caused by the temperature gradient at the substrate surface. The induced convection would lead to values of H much larger than that derived solely from thermal conduction alone. An order of magnitude estimate of H can also be made from information obtained from processes of a nature similar to the one studied here. In a study of laser-enhanced electroplating of copper in a 0.05M $CuSO_4$/1.0M H_2SO_4 bath (14), a limiting current density of 18 A/cm^2 was obtained in the area illuminated by an Ar^+ laser. Assuming a value of 1.0×10^{-5} cm^2/s for the diffusion coefficient of the cupric ion, the 18 A/cm^2 limiting current density produces a thickness of 0.053 μm for the mass-transfer boundary layer (14). For developed laminar and turbulent flows, thickness of the mass-transfer boundary layer is equal to the −1/3 power of the Schmidt number, Sc, defined as the ratio of kinematic viscosity to diffusion coefficient, times thickness of the hydrodynamic boundary layer. Similarly, thickness of the thermal boundary layer is equal to the −1/3 power of the Prandtl number, Pr, defined as the ratio of kinematic viscosity to thermal diffusivity, times thickness of the hydrodynamic boundary layer. The Sc/Pr ratio for aqueous solutions at room temperature is about 150, and, therefore, under similar hydrodynamic conditions the thermal boundary layer is approximately five times as thick as the mass-transfer boundary layer. Assuming that the hydrodynamics of the copper plating system is representative of that in our etching system, the thermal boundary layer is thus estimated to be 0.27 μm thick for the laser etching system. Such a thermal boundary layer thickness would produce a value of 55 cal/cm^2-s-°C for the heat transfer coefficient, H. As seen from Fig. 2, significant surface cooling will occur for such a large H value.

So far in our discussion we have attributed only conduction and convection in the solution phase to the evaluation of H, and have not taken into account the effects due to the presence of a film on the ferrite surface. In the case

of the laser-enhanced plating, a thermally conductive metal film was generated as the substrate-liquid interface, and convection in the plating bath determined the heat dissipation rate. Although there was significant cooling at the electrode surface, the temperature could still exceed the boiling point of the bath, and bubbles were generated. On the other hand, no boiling of the KOH etchant solution was observed during etching of the ferrite surface although the laser power densities were, in general, higher than those used in the plating experiments. The absence of gas bubbles during the etching experiments could be explained by the presence of a film of high thermal resistance between the ferrite surface and the etchant. With the introduction of such a film, the heat transport process is dominated by conduction through this film, and the value of H is drastically lowered. Although we could not experimentally verify the presence of such a film, the absence of gas bubbles as well as the good agreement between the width of the etched grooves and the width of the melted grooves computed under the no-loss assumption, illustrated in Fig. 12 (see later paragraphs for discussion), indicates that during the etching process the ferrite surface behaved close to an insulating plane. These facts can be considered as indirect evidence for the presence of a fused layer of high thermal resistance on the ferrite surface, when etched by KOH under the assistance of laser energy. The surface cooling effect on the temperature is thereby excluded in the discussion of both the model and experimental results.

Under the assumption of no heat loss into the liquid medium, the last boundary condition becomes

$$\frac{\partial T}{\partial z} = 0 \quad \text{at } z = 0$$

The temperature rise at the ferrite surface with $\Theta = 0$ in Eq. [6] is represented by

$$T(X, Y, 0, \tau) = \frac{P}{\pi\kappa\lambda}\int_0^{\tau} \frac{1}{1+4\phi} e^{\alpha^2\phi}\,\mathrm{erfc}\,(\alpha\sqrt{\phi})\, e^{-\frac{[(X-\mu\phi)^2+Y^2]}{1+4\phi}}\, d\phi \qquad [7]$$

Equation [7] is nearly identical to a previously published formulation (15). The upper bound of integration in Eq. [7] is "τ", while the upper bound of integration in the formulation appearing in Ref. (15) is "∞." The author of Ref. (15) assumes that the laser beam is turned on at $\tau = -\infty$, *i.e.*, an initial position of the laser beam at $X = -\infty$ as viewed from our coordinate system, and thus obtained the steady-state solution which in turn can be considered as the temperature-time correlation for a ferrite particle infinitely far away from the initial beam position. Our formulation takes into account the finite distance between the position of the ferrite particle of interest and the initial beam location, and thus has a time-dependence in the formula. We believe that our formulation is more realistic, and that the inherent time-dependence of the temperature in Eq. [7] can be important in considering the temperature at the edges of a substrate of finite size. Additionally, the spatial coordinates used in Ref. (15) are located on the moving substrate, and are thus moving with respect to the stationary laser beam; while our formulation is based on spatial coordinates which are stationary with respect to the laser beam and are thus moving with respect to the substrate. As a result, $T(x, y, 0, \tau)$ in Ref. (15) represents the temperature measured at time τ for a particle initially located at $(x, y, 0)$; while in our model, $T(x, y, 0, \tau)$ represents the temperature at time τ measured at a fixed point $(x, y, 0)$ in space. Different ferrite particles occupy the spot $(x, y, 0)$ at different times. Above a certain τ value a pseudo steady-state temperature distribution develops, and the integration in Eq. [7] would be independent of τ. The following discussion is based on the steady-state temperature.

The computed steady-state temperature distribution along the Y-axis for a stationary substrate using Eq. [7] is the same as that given in Fig. 2 for $H = 0$. The temperature rise is proportional to the laser power, as is indicated by

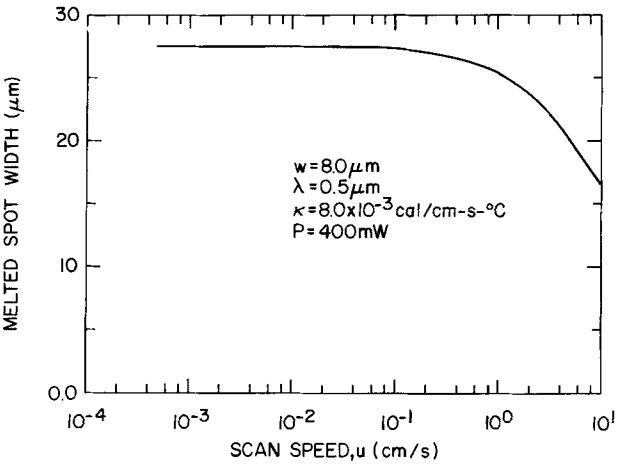

Fig. 3. Effect of scan speed on the melting boundary (computed)

Eq. [7]. The effects of scan speed and laser power are illustrated in Fig. 3 and 4, respectively. The selected ordinate is the width of the melted grooves, which is twice the y value where the temperature is at the melting point of ferrite. We feel that this ordinate is more effective in presenting the key features of our model, although we do not have experimental evidence to directly link the etching and melting phenomena. A value of 1565°C, which is the melting point of Fe_2O_3, is assigned as the melting point of ferrite. For the substrate moving in the X direction, the temperature distribution is symmetric with respect to the X axis, but is asymmetric with respect to the Y axis. The asymmetry is caused by the term, $\mu\,\partial\Psi/\partial X$, in Eq. [3]. The dimensionless group μ indicates the contribution of convection as a heat transport mechanism as compared to that of thermal diffusion. Large μ means that more heat is carried along with the substrate instead of being allowed to dissipate laterally. As a result, the hottest spot shifts toward the leading edge of the beam as the scan speed increases. Additionally, the peak temperature decreases as the scan speed increases, a result expected from residence time considerations. Nonetheless, the magnitude of the thermal diffusivity for ferrite, 6.03×10^{-3} cm^2/s (16) and of the characteristic length (beam waist, w) renders a significant variation of temperature distribution as well as a significant decrease of the melted groove size only for scan speeds exceeding ~1 cm/s. This is verified in Fig. 3. In Fig. 4 it is seen that for laser power levels higher than 300 mW a linear correlation between the melted spot size and the laser power is observed. For a point heat source, $T \sim P/r$ where r is the distance from the point source, and the melted spot size would be proportional to the laser power. The point source assumption is more valid for larger melted spots, *i.e.*, higher laser power levels. At lower power levels, the point source assumption no longer holds true and the linear correlation is not observed. As the power is lowered, the area

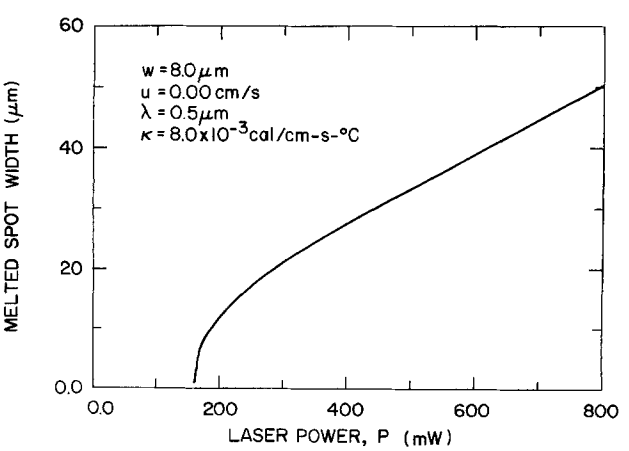

Fig. 4. Effect of laser power on the melting boundary (computed)

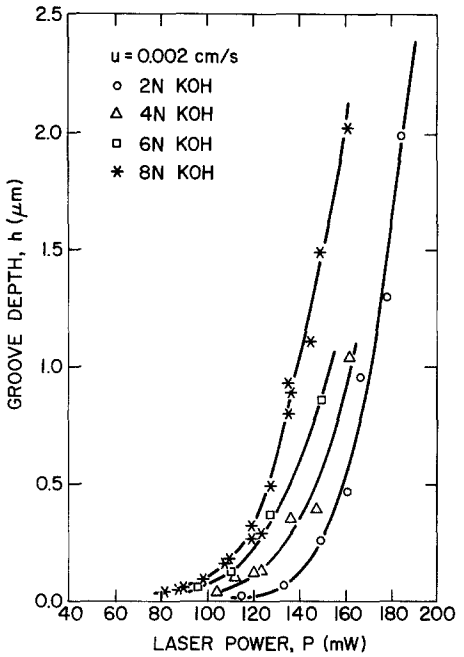

Fig. 5. Experimental data for groove depth-laser power correlation as a function of KOH concentration (low laser power case).

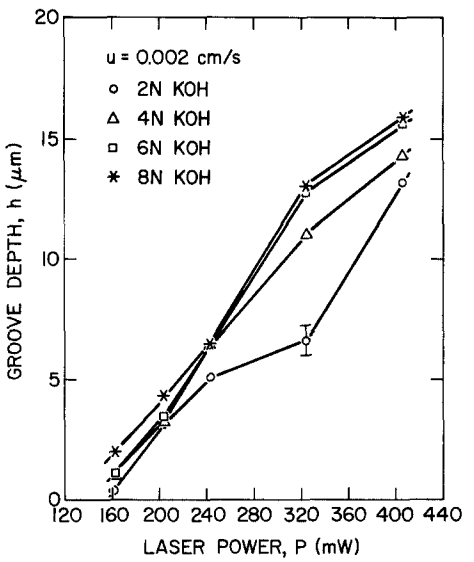

Fig. 6. Experimental data for groove depth-laser power correlation as a function of KOH concentration (moderately higher laser power case).

with temperature exceeding the melting point shrinks drastically, and a sharp drop-off of the melted spot size is seen.

Experimental Results and Discussion

Preliminary etching experiments were performed in KOH solutions of concentration ranging from 0 to 8*N*. The upper bound of 8*N* was selected arbitrarily. It was found that when the KOH concentration was below ~2*N*, etching was accompanied by bubble formation, with higher nucleation frequency for less concentrated etchant. Boundaries of etched patterns were irregular and the process was uncontrollable. As the KOH concentration exceeded 2*N*, the etching process became bubble-free, and boundaries of etched grooves were well defined. Accordingly, our etching experiments were done only in 2-8*N* KOH solutions. Under normal experimental conditions, only dissolution of the ferrite took place, and we did not detect the formation of tiny solid particles either during or after the etching experiment. Only in a few etching experiments performed under very high laser power, high KOH concentration, and low scan speed conditions, chipping of the ferrite substrate was observed.

The knife-edge technique (17) was used to measure the 1/*e* beam radius. The 1/*e*-beam radius was 8.0 μm for the 5 times objective lens. When the substrate was not moving, the threshold laser power for visually detectable melting of ferrite in air was found to be 144 ± 1 mW. Attempts to obtain reproducibly the threshold laser power for melting ferrite in water were unsuccessful because of excessive bubble formation. Assuming a value of 8.0×10^{-3} cal/cm-s-°C for the thermal conductivity of ferrite and a value of 6.03×10^{-3} cm^2/s for the thermal diffusivity of ferrite (16), our model calculates a maximum temperature of 1440°C for a laser power of 144 mW. In KOH solution etching of ferrite was observed at power levels below this melting threshold, indicating that melting of ferrite may not be a necessary condition for etching to take place. Similar behavior was observed in etching of $PbTiO_3$ (5).

The influence of KOH concentration on the correlation between the groove depth and the laser power is illustrated in Fig. 5 and 6, covering, respectively, the very low end and the moderately high end of the laser power spectrum in our experiments. The groove depth increases with increasing laser power and, to a lesser extent, with increasing etchant concentration. Less power is required for etching to proceed in more concentrated etchant; and at a fixed power, higher etch rate is obtained for more concentrated etchant. Data in Fig. 5, appear to bear the mark of Arrhenius-type kinetics. Data in Fig. 6 show a linear relation between the groove depth and the laser power.

SEM micrographs are shown in Fig. 7 to illustrate the two types of profiles for the etched groove observed in our experiments. The smooth bell-shaped profile usually associated with high etchant concentration, low scan speed conditions; ridge formation at the bottom of the grooves usually took place when etching experiments were done under low etchant concentration, high laser power, high scan speed conditions. The similarity between the groove shape and the shape of the temperature profiles in Fig. 2 is brought to readers' attention, although no attempt is made here on quantitative comparison. Energy dispersive analysis of x-rays (EDX) results indicated that the ridge substance was Mn-Zn-ferrite. At the same scan speed and laser power, the grooves etched in 2*N* KOH are shallower and rougher compared to those etched in 6*N* KOH.

Shown in Fig. 8 is the $u \times h$ (scan speed × groove depth) *vs.* u (scan speed) correlation for three different power levels in 2*N* KOH. The smoothly etched grooves are bell-shaped and "h" refers to the depth reading at the valley, where $y = 0$. For each point on the x-axis, the period over which it is under laser heating is approximately $2w/u$. Therefore, the term $uh/2w$ can be considered as a "time-averaged etch rate." It should be pointed out that each point on the x-axis is experiencing constantly varying temperatures during the period over which it stays within the heating zone of the laser beam. The calculations based on our model show that over the range of 0.001-0.5 cm/s for the scan speed, where we operated our experimental system, the temperature was practically independent of the scan speed. Consequently, the product of the scan speed "u," which is inversely proportional to the residence time, and the groove depth "h" should be a constant for all grooves etched under the same power but at different scan speeds, provided that the etching process is purely kinetics controlled and the area receiving laser power changes little with the evolution of the groove shape. This constant, when divided by $2w$, refers to a time-averaged or, in essence, a temperature-averaged, etch rate, instead of the etch rate at the peak temperature. One should not attempt to extract information on etch kinetics from profiles of grooves etched by a scanning laser beam. A constant value for $u \times h$ is observed in Fig. 8 for the curve with the lowest laser power (173 mW); with a value of 4.3 μm/s for the average etch rate, $uh/2w$. As the laser power increases, $u \times h$ no longer stays constant, being smaller for smaller scan speed. Shown in Fig. 9 is the $u \times h$ *vs.* u correlation for four KOH concentrations, at a fixed laser power of 324 mW. Since the selected power level is moderately high, we do not obtain a constant for $u \times h$. For the less concentrated etchants (2*N* and 4*N*), $u \times h$ increases with increasing scan speed. Similar behavior is observed for the more concen-

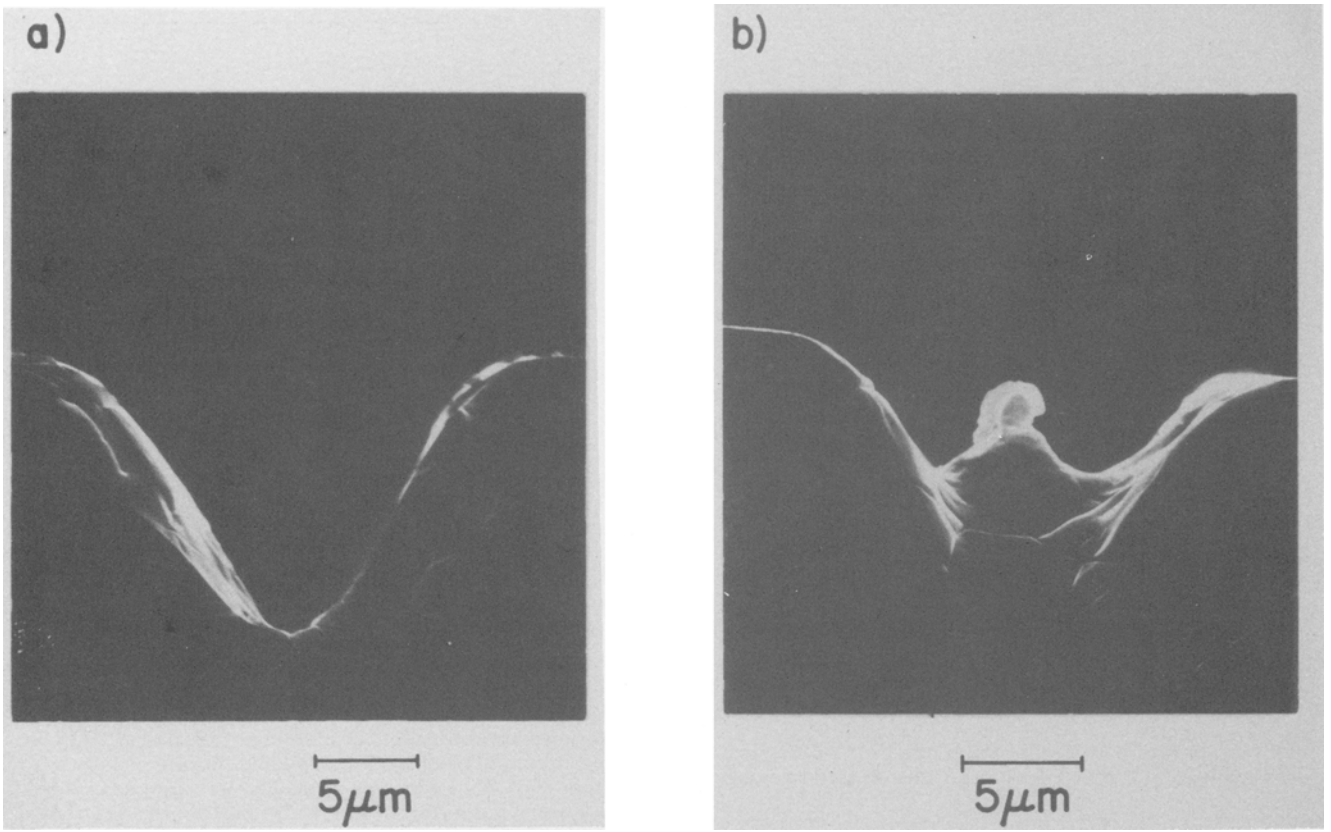

Fig. 7. SEM micrographs of etched grooves: (a) A smooth bell-shaped groove; laser power = 324 mW, scan speed = 0.02 cm/s, KOH concentration = 6*N*. (b) A rough groove with ridge formation; laser power = 405 mW, scan speed = 0.02 cm/s, KOH concentration = 2*N*.

trated etchants (6*N* and 8*N*), except that a drop of $u \times h$ value is seen at high scan speeds.

Deviation from a constant $u \times h$ value can be partially explained from geometric considerations. As the etching process progresses, the groove surface deviates further from the initial planar geometry and the surface area for receiving the beam energy increases. As a result, the energy density decreases and so does the etch rate. This geometric factor, if it plays a significant role, leads to a smaller $u \times h$ value for a smaller scan speed. Additionally, as the groove grows deeper with increasing laser power at lower scan speeds, the reaction gradually becomes mass transport controlled and consequently $uh/2w$ no longer represents the etch kinetics.

We have mentioned earlier that even at the boiling point of the aqueous KOH etchant, chemical etching did not take place. At low laser power levels where etching is not experimentally observed, the computed surface temperature is already much higher than the boiling point of the aqueous etchant. Consequently it is reasonable to assume that under laser illumination conditions the chemical environment at the ferrite surface must be different from simply the boiling etchant. This argument and the fact that no boiling was observed in concentrated etchant lead us to believe that an intermediate layer of substance exists between the aqueous etchant and the solid ferrite. A logical picture would be the presence of a thin layer of molten (dehydrated) KOH on the ferrite surface. Either the molten KOH film or the film resulting from the KOH-ferrite interaction may be a high resistance for dissipating heat into the aqueous etchant, and the ferrite surface would behave as an insulating plane. The ferrite-molten KOH interface can thus be at a high temperature, as was calculated from

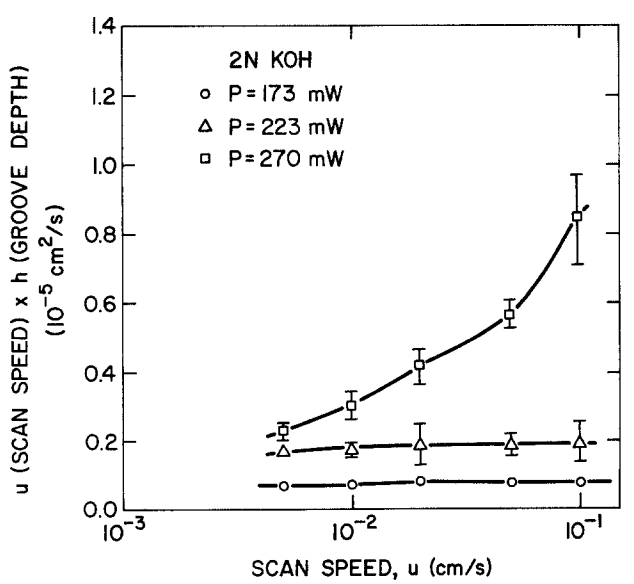

Fig. 8. Experimental $u \times h$ *vs. u* correlation at different laser power levels.

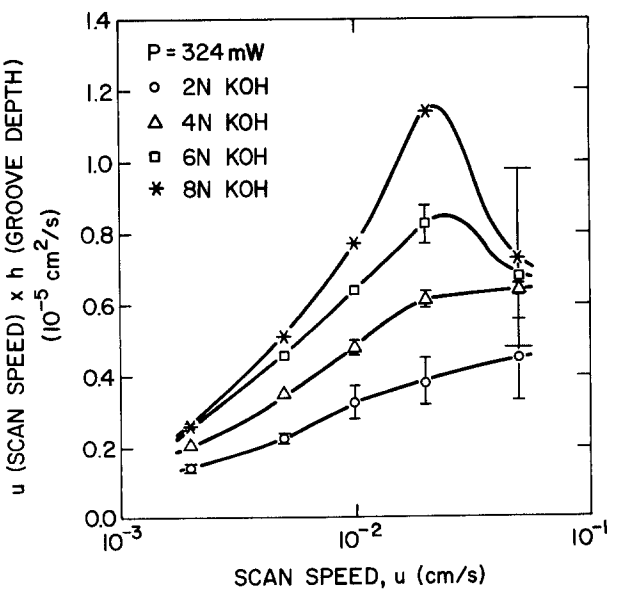

Fig. 9. Experimental $u \times h$ *vs. u* correlation in KOH solutions of different concentrations.

the model, for etching to proceed; while the aqueous etchant has contact with the cooler side of the film so that boiling does not occur. Only when there is not enough KOH to form such a film over the entire etched area, which occurs in dilute etchants, water comes in contact with hot ferrite surface and boiling ensues.

We propose the following physical phenomena for qualitative interpretation of the experimentally observed etching behavior: during the etching process KOH in the bulk etchant needs to be transported, mainly through diffusion, to the ferrite surface. Under laser illumination the ferrite surface temperature rises and this induces a change in the local chemical environment, the exact nature of which is unknown to us. One possibility is the localized water removal to generate a surface layer of molten (or extremely concentrated) KOH. When a threshold temperature (*i.e.*, laser power) is reached, the chemical environment on the ferrite surface becomes reactive with the solid ferrite substrate and etching takes place. The melting point of KOH is 360°C, which is much lower than the melting point of the ferrite. Consequently this chemical route might very well not require that the substrate temperature reach its own melting point, and should be the controlling mechanism under low power conditions. Since the water content is lower for the more concentrated etchant, less power is required to initiate etching in the more concentrated etchant, as we have observed in the experiment. On the other hand, under high laser power conditions, reaction between molten ferrite and the etchant is also a very likely reaction path. Due to differences in their nature, the individual rate of these two reaction mechanisms may be quite different. Both reaction mechanisms, if in effect, would contribute to the experimentally observed etching behavior, but the individual contribution cannot be resolved from the experimental data. The fact that no solid particles were observed in the etching experiments indicates that the etching reaction generates product species (probably through complex formation) that are soluble, even at room temperature, in the etchant. These soluble species need to be transported out of the grooves and into the bulk solution. Buildup of the reaction product inside the groove may be expected to eventually stop the etching.

As stated in earlier paragraphs, a ferrite particle being etched experiences a time-varying temperature during the etching process. Under scanning conditions, a significant variation in surface temperature and etch rate takes place over a period of $\sim 2w/u$. It can be expected that the solubility of the nongaseous reaction product increases with increasing temperature. Therefore, an extremely high instantaneous surface concentration for the reaction product can be sustained when the particle moves under the beam center. This surface concentration is determined by the balance of the etch rate and the mass transport rate out of the groove. Once the particle passes the beam center, the temperature starts to drop and the surface becomes supersaturated with the reaction product. As a result, recrystallization takes place. Since the center of the groove is the hottest spot and has the highest degree of supersaturation, the recrystallized substances cluster around the center of the groove, as is demonstrated in Fig. 7b. Additionally, higher laser power facilitates the surface concentration rise, while faster scan allows less time for the reaction product to diffuse into the bulk solution. Therefore, formation of ridges at the groove bottom occurs under such conditions. The drop-off of $u \times h$ value at high scan speed as seen in Fig. 9 can be attributed to the short residence time, resulting in a significant amount of recrystallized substances, as is indicated by the large range for the error bars. The fact that it is easier to observe the ridge formation in more diluted etchant, for which the etch kinetics is slower, can only be explained by the assumption that the reaction product is more soluble (stable) in the more concentrated KOH solution.

The influence of laser power, scan speed, and KOH concentration on the width of the etched grooves is illustrated in Fig. 10-12. Generally speaking, KOH concentration has little effect on the groove width, except at very low power levels (< 200 mW) where the difference in etch rate is more pronounced. The variation of the groove width with scan

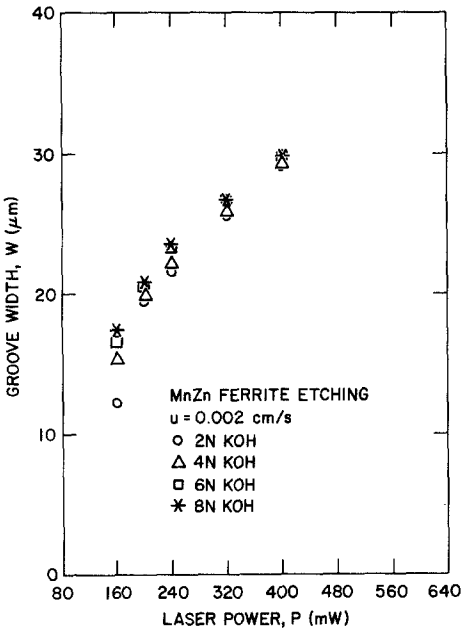

Fig. 10. Experimental data of the effect of KOH concentration on the groove width-laser power correlation.

speed becomes detectable when the scan speed is larger than 0.01 cm/s (Fig. 11). Faster scans result in narrower grooves. However, the influence of etchant concentration and scan speed on the magnitude of the width variation is relatively small as compared to the effects of laser power. As is shown in Fig. 12, the groove width varies in a linear fashion with the laser power, except at low power levels (< 200 mW) where a significant drop-off is seen. Furthermore, the width "*W*" *vs.* power "*P*" curve in Fig. 12 follows closely the corresponding curve for ferrite melting, although these experimental data cannot be fitted successfully by a unique "threshold etching temperature" over the entire power range. The trend observed in Fig. 12 can be qualitatively explained by the proposed etching mechanism, namely, the superimposition of etchant (most probably molten KOH)-solid ferrite interaction and etchant-molten ferrite interaction. The etchant-solid ferrite reaction is expected to dominate at low power levels, and this is demonstrated by the large positive deviation observed in Fig. 12 for power levels less than 240 mW, particularly below 160 mW where melting of ferrite is not expected. As the

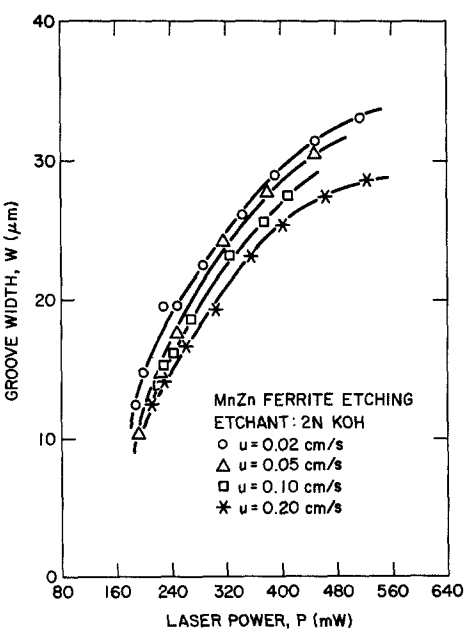

Fig. 11. Experimental data of the effect of scan speed on the groove width-laser power correlation.

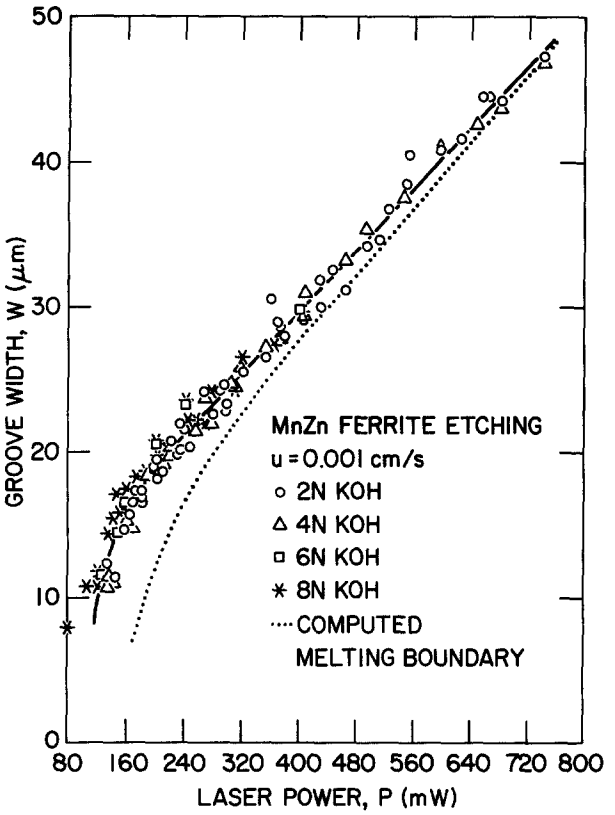

Fig. 12. Comparison of experimental groove width-laser power correlation with computed melting boundary.

power is increased and melting of ferrite occurs, the etchant-molten ferrite reaction dominates and the experimental curve merges into the computed melting boundary curve.

Summary

We have carried out experiments for understanding of the laser-assisted etching of Mn-Zn-ferrite in KOH solutions. In the absence of the laser beam the etching process did not take place even at the boiling point of the selected etchant. A minimum KOH concentration of ~2*N* is required for a controllable bubble-free etching process. The threshold laser power for etching was found to be smaller than that required for visually detectable melting of ferrite to occur in air, and decreased with increasing etchant concentration. Within the range of 2-8*N* for KOH concentration, the depth of the etched grooves increased with increasing laser power, decreasing scan speed, and increasing KOH concentration. Except for very high power levels where chipping occurred, no solid particles were observed during the etching process. This leads us to believe that soluble species are generated from the etching process, and transport of the etchant and of the reaction product(s) can influence the etch profiles. Evidence of mass transport limitation on the average etch rate was observed under low KOH concentration, high power, and low scan speed conditions. Under high scan speed, high laser power, and low etchant concentration conditions, ridge formation at the valley of the etched grooves was detected. It is postulated that the short residence time under high scan speed conditions results in supersaturation of reaction product as well as crystallization inside the etched grooves. Extracting information on the etching kinetics based on the measured groove depth was inappropriate because the etching process was not fully kinetics controlled under the chosen experimental conditions and each spot on the substrate was subject to time-varying temperatures during the period of etching. The width of the etched grooves increased with increasing laser power, but was relatively insensitive to the scan speed and the KOH concentration. Good agreement between the width of the etched grooves and the width of the melted grooves computed under the no-loss assumption points to the possible presence of a thin layer of fused material with high thermal resistance between the ferrite and the liquid medium. Findings from experiments on laser-assisted etching of ferrite can be qualitatively explained by the following events: formation, at and above a threshold temperature, of an active chemical environment on the Mn-Zn-ferrite surface for the initiation of the etching process; more concentrated etchant allows more abundant supply of the reactive species and requires less heat input to reach the active state. Etching of ferrite occurs as a result of the reaction between the active etchant (possibly fused KOH) and either solid ferrite or molten ferrite, depending on the power input. The etching process generates soluble product species and the profiles of the etched patterns are strongly influenced by the mass transport characteristics of the etching system.

Acknowledgments

The authors wish to thank G. Egbert of IBM Rochester, Minnesota, for supplying the Mn-Zn-ferrite materials and for invaluable discussions through the course of this study. The authors would also like to express their gratitude to K. Mitchell and P. Bailey for their efforts in SEM and EDX analysis.

Manuscript submitted Feb. 1, 1988; revised manuscript received July 12, 1988.

IBM T. J. Watson Research Center assisted in meeting the publication costs of this paper.

LIST OF SYMBOLS

C_p	heat capacity, cal/g-°C
D	thermal diffusivity, cm²/s
G	Green's function shown in Eq. (4)
H	heat transfer coefficient, cal/cm²-s-°C
h	depth of the etched grooves, μm
I	laser beam intensity at (x, y, z), W/cm²
P	laser power, W
r	distance from a point heat source, cm
T	temperature rise above room temperature, °C
t	time, s
u	scan speed, cm/s
W	width of the etched grooves, μm
w	1/e beam radius, μm
X	dimensionless coordinate
x	dimensional coordinate corresponding to X, μm
Y	dimensionless coordinate
y	dimensional coordinate corresponding to Y, μm
Z	dimensionless coordinate
z	dimensional coordinate corresponding to Z, μm

Greek characters

α	dimensionless group defined as w/λ
ΔT	maximum temperature rise under surface absorption condition, °C
κ	thermal conductivity, cal/cm-s-°C
λ	absorption depth, μm
μ	dimensionless group defined as uw/D
ρ	density, g/cm³
τ	dimensionless time defined as tD/w^2
Θ	dimensionless group defined as wH/κ
ϕ	integration variable in Eq. [5] and [6]
Ψ	dimensionless temperature rise defined as $T/\Delta T$

REFERENCES

1. D. Bäuerle, "Chemical Processing with Laser," Vol. 1, p. 162, Springer Series in Materials Science, Springer-Verlag, Heidelberg (1986).
2. A. E. Willner, D. V. Podlesnik, H. Gilgen, and R. M. Osgood, in "Photon, Beam, and Plasma Stimulated Chemical Processing at Surfaces," V. M. Donnelly, I. P. Herman, and M. Hirose, Editors, p. 403, *Mater. Res. Soc. Symp. Proc.*, **75,** (1987), and references therein.
3. R. J. von Gutfeld and R. T. Hodgson, *Appl. Phys. Lett.*, **40,** 352 (1982).
4. E. F. Krimmel, A. G. K. Lutsch, R. Swanepoel, and J. Brink, *Appl. Phys. A*, **38,** 109 (1985): F. V. Bunkin, B. S. Lukyanchuk, G. A. Shafiev, E. K. Kozlova, A. I. Portniagin, A. A. Yeryomenko, P. Mogyorosi, and J. G. Kiss, *ibid.*, **37,** 117 (1985).
5. T. Shiosaki, M. Tanizawa, H. Kamei, and A. Kawabata, *Jpn. J. Appl. Phys.*, **22,** Suppl. 22-2, 109 (1983).

6. "Kirk-Othmer Encyclopedia of Chemical Technology," Vol. 9, p. 881, John Wiley & Sons, Inc., New York (1980).
7. A. Broese van Groenov, P. E. Bongers, and A. L. Stuijts, *Mater. Sci. Eng.*, **3**, 317 (1968-1969).
8. S. Kawado, *Jpn. J. Appl. Phys.*, **9**, 24 (1970).
9. M. Uemura, T. Hyono, M. Umeno, and H. Kawabe, *J. Mater. Sci.*, **21**, 1341 (1986).
10. M. J. N. Pourbaix, "Atlas of Electrochemical Equilibria in Aqueous Solutions," Oxford University Press, New York (1966).
11. H. S. Carslaw and J. C. Jaeger, "Conduction of Heat in Solids," 2nd ed., pp. 11 and 89, Oxford University Press, New York (1959).
12. *ibid.*, p. 358.
13. "Handbook of Chemistry and Physics," 63rd ed., p. E-10, (CRC Press Inc., Boca Raton, FL (1982-1983).
14. L. T. Romankiw, M. H. Gelchinski, R. E. Acosta, and R. J. von Gutfeld in "Electroplating Engineering and Waste Recycle, New Developments and Trends," (PV 83-12) D. D. Snyder, U. Landau, and R. Sard, Editors, p. 66, The Electrochemical Society Softbound Proceedings Series, Pennington, NJ (1982).
15. D. J. Sanders, *Appl. Opt.*, **23**, 30 (1984).
16. G. Egbert, IBM Corporation, Rochester, MN, Private communication.
17. Y. Suzaki and A. Tachibana, *Appl. Opt.*, **14**, 2809 (1975).

Production of Fluorine by the Electrolysis of Calcium Fluoride-Containing Tetrafluoroborate Melts

Gleb Mamantov* and T. M. Laher

Department of Chemistry, University of Tennessee, Knoxville, Tennessee 37996-1600

ABSTRACT

Tetrafluoroborate melts have been shown to be viable electrolytes for the electrochemical production of fluorine from dissolved CaF_2. The anode reaction at pyrolytic graphite electrodes apparently involves the oxidation of BF_4^- and/or F^- to yield BF_3 and F_2. LiF may be used to trap BF_3; the resulting $LiBF_4$ may be reused in the bath. Observed anode current efficiencies are generally on the order of 50-60% at an optimum anode current density of 40 mA/cm^2. The cathode reaction at tin and/or zinc cathodes involves the reduction of Ca^{2+} to the metal along with the reduction of alkali metal ions to the respective metals. The presence of zinc in the cathode pool appears to favor the deposition of calcium over that of alkali metals.

Fluorine is currently produced by the electrolysis of KF-HF (50/50 mole percent [m/o]) melts at temperatures of *ca.* 150°C (1). These materials are produced from naturally occurring minerals containing CaF_2, most notably fluorspar (CaF_2). It would be more desirable to produce fluorine directly from CaF_2. Due to the reactivity of fluorine, especially at elevated temperatures, it is necessary to carry out the electrolysis for the production of fluorine using relatively low liquidus temperature electrolytes in which CaF_2 is at least partially soluble. This requirement narrows the field of prospective electrolytes to relatively low melting alkali fluoride mixtures such as the LiF-NaF-KF eutectic and various melts containing tetrafluoroborate, all of which have liquidus temperatures below 500°C (2, 3). No reports could be found in the literature for the electrolytic production of fluorine from melts containing CaF_2. In the mid-1960s, Mastrangelo reported an electrolytic method for the production of fluorine from molten $NaBF_4$ (4). In this method, carbon or gold anodes were used to produce F_2 by the oxidation of BF_4^-, and Na^+ was reduced at a lead cathode pool to give a Na-Pb alloy which could be used in the production of tetraethyl lead. Some problems were encountered with the tetrafluoroborate melts, especially with melts containing $LiBF_4$, in that BF_3 is evolved during electrolysis and it is necessary to trap BF_3, preferentially by a method which recycles BF_3 back into the electrolyte (4). $LiBF_4$ is known to undergo spontaneous decomposition to LiF and BF_3 at 325°C (5). In this paper we discuss a method for the electrolytic production of fluorine from tetrafluoroborate melts containing CaF_2 at temperatures of 315°-375°C.

Experimental Section

Electrochemical cell.—The electrochemical cell (Fig. 1) consisted of a nickel cell body containing an alumina crucible (Coors AD 998, 36 mm id). The crucible which contained the electrolyte was separated from the cell body by means of a larger alumina crucible of slightly smaller diameter than the inside of the nickel cell body. The purpose of the second crucible was to protect the heated portion of the cell body from attack by hot fluorine gas. The top flange of the cell body was fitted with a center port equipped with a Swagelok fitting for introduction of the anode or an addition tube through which the cathode metal pool was added, and with four ports equipped with Cajon ultra-torr fittings for introduction of the gas en-

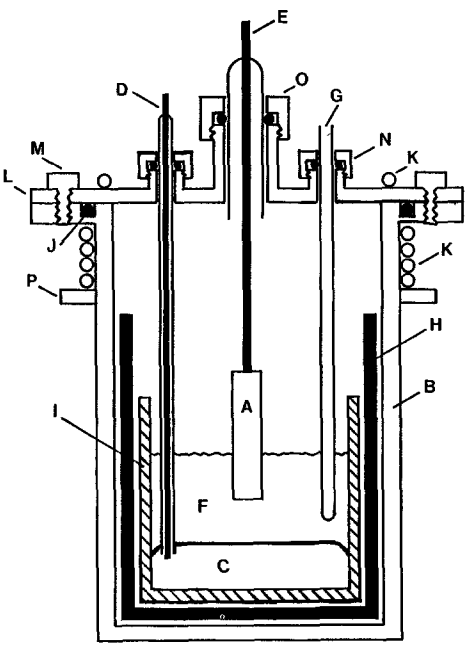

Fig. 1. Electrochemical cell used for electrolysis of tetrafluoroborate melts containing CaF_2. The parts of the cell are listed: (A) anode substrate, (B) Ni cell body, (C) cathode metal pool, (D) Ni cathode contact lead, (E) Ni anode contact lead, (F) tetrafluoroborate melt, (G) thermocouple well (alumina tube), (H) alumina insert, (I) alumina crucible containing melt, (J) Viton O-ring, (K) cooling coils, (L) Ni top flange, (M) bolt, (N) Cajon fitting, (O) specially adapted Swagelok fitting, and (P) Ni support ring. Dimensions are not to scale.

* Electrochemical Society Active Member.